Iranian Journal of Hydrogen & Fuel Cell 1(2020) 45-60

Iranian Journal of Hydrogen & Fuel Cell

IJHFC

Journal homepage://ijhfc.irost.ir

Lattice Boltzmann simulation of water transfer in gas diffusion layers with porosity gradient of polymer electrolyte membrane fuel cells with parallel processing on GPU

Mohammad Habiballahi[1], Hasan Hassanzadeh[1*], Mohammad Rahnama[2], Seyed Ali Mirbozorgi[1] and Ebrahim Jahanshahi Javaran[3]

[1] Department of Mechanical Engineering, University of Birjand, Birjand, Iran.
[2] Department of Mechanical Engineering, Shahid Bahonar University of Kerman, Kerman, Iran.
[3] Department of Energy, Graduate University of Advanced Technology, Kerman, Iran.
* P.O.B. 97175/615

Article Information

Article History:

Received:
2020-02-05
Received in revised form:
2020-04-23
Accepted:
2020-04-25

Keywords

PEM fuel cell
Lattice Boltzmann method
Gas diffusion layer
Two-phase flow
GPU parallel processing
Porosity gradient

Abstract

This study used the lattice Boltzmann method (LBM) to evaluate water distribution in the gas diffusion layer (GDL) of cathode PEM fuel cells (PEMFCs) with porosity gradient. Due to the LBM's capability of parallel processing with a GPU and the high volume of computing necessary, especially for small grids, the GPU parallel processing was done on a graphics card with the help of CUDA to speed up computing. The two-phase flow boundary conditions in the GDL are similar to the water transfer in the GDL of the PEMFCs. The results show that capillary force is the main cause of water transfer in the GDL, and gravity has little effect on the water transfer. Also, the use of GPU parallel processing on the graphics card increases the computation speed up to 17 times, which has a significant effect on running time. To investigate the gradient of porosity of GDLs with different porosity gradients, but the same average porosity coefficient and the same particle diameter have been evaluated. The simulation results show that the GDL with a 10% porosity gradient compared to the GDL with uniform porosity results in a 20.2% reduction in the amount of liquid water in the porous layer compared to the GDL with uniform porosity. Hence, increasing the porosity gradient of the GDL, further decreases the amount of liquid water in the porous layer. So, for the GDL with a porosity gradient of 14% this decrease is 29.8% and for the GDL with porosity gradient 18.5% this decrease is 38.8% compared to the GDL with uniform porosity.

1. Introduction

Water management is considered as one of the major challenges of PEMFCs, in particular at high densities on the cathode side. The dehumidification of PEMFCs' inlet gases and the production of water in the cathode catalyst provide the conditions for two-phase flow in the GDL cathode. At high densities, inadequate water withdrawal from the cathode electrode increases the resistance to oxygen transfer to the cathode catalyst, which results in a decrease in oxygen concentration in the catalyst and a consequent decrease in the efficiency of PEMFCs [1-3].

*Corresponding author:h.hassanzadeh@birjand.ac.ir

Over the past decades, numerous articles have been presented to investigate water management in different parts of PEMFCs. One of the most common methods for water management is the membrane dehumidification of inert PEMFCs. Humidification of inlet gases to PEMFCs prevents membrane drying at high densities. However, the introduction of high saturation reactions from water into PEMFCs coupled with the production of water in the catalyst can lead to the occurrence of a flooding phenomenon at the cathode electrode, which is associated with a decrease in the PEMFCs' efficiency. Another method to improve water management is with hydrophobia electrodes, and various researchers have shown that GDL hydrophobia plays an important role in the transfer of liquid water into the GDL [4, 5]. Also, changes in the porosity structure of the GDL can enhance water management in PEMFCs [6].

The use of GDL with porosity circuits also improves water management in PEMFCs and has been discussed in numerous articles [7, 8]. Moreover, Grew et al. [9] applied a one-dimensional analytical model to model the GDL with the porosity gradient. They assumed the GDL was parallel layers with different porosities and stated that parts of it can even be filled with water; so, the GDL cannot have a uniform porosity. Shi et al. [10] also investigated the effect of porosity changes in the GDL on the performance of electrolyte membrane fuel cells PEMFCs with a one-dimensional model. Their results show that, at high current densities, the performance curve of electrolyte membrane fuel cells PEMFCs with the GDL fits better with the experimental results. In a three-dimensional, biphasic and non-isothermal model, Hong et al. [11] investigated the effect of porosity circulating gas permeable layers on the performance of PEMFCs with three types of parallel, spiral, and connective channels. Their results show that the use of GDL with porosity circuits for water transport in electrolyte membrane fuel cells PEMFCs with parallel and spiral channels is better than in the connecter one. Lee et al. [12] investigated the effect of porosity gradient on the GDL on the phenomenon of waterlogging, oxygen penetration, and efficiency of electrolyte membrane fuel cells PEMFCs. Their results show that the amount of saturation and oxygen concentration depends on the structure of the porosity in the GDL. Tang et al. [13] investigated GDL and micro-porous layer (MPL) characteristics, including how porosity, hydrophobia, and permeability changes affected water management and efficiency of electrolyte membrane fuel cells PEMFCs. The results show that the MPL increases the efficiency of electrolyte membrane fuel cells PEMFCs at high density. Park et al. [14] investigated the effect of GDL structure porosity on capillary pressure in the transient and permanent state. The results also show that the gradient porosity structure improves the performance of PEMFCs, especially in the relative humidity range of 50 to 100%, while increasing the membrane moisture content. Zhang and coworkers [4] also investigated the effect of porosity GDL deformation on the amount of saturation and discharge of electrolyte membrane fuel cells PEMFCs. They showed that a GDL with linear porosity distribution and the highest gradients has the best performance for PEMFCs by comparing three s with different average porosity coefficients. Chen et al. [15] investigated the two-phase flow in a GDL with a porosity gradient in PEMFCs. Using a multiphase mixture model, they showed that gas permeability layers with a porosity gradient lead to a better transfer of liquid water and an increase in oxygen transfer from the GDL.

The evaluated articles show that the use of gas permeation layers with Porosity gradient has a positive effect on water management and performance of Polymer fuel, this can be further modeled through the pore scale modeling of the GDL.

In the last decade, numerous articles have been published on water diffusion in the GDL at the pore scale. Kim et al. [16] investigated water transfer in a MPL and GDL of a Polymer fuel cell using the LBM. Their results show that the use of MPL improves water management in the GDL in electrolyte membrane fuel cells PEMFCs. Using the LBM, Molaeimanesh et al. [17] investigated the effect of using polytetrafluoroethylene (PTFE) to dehydrate the GDL. The researchers simulated a four-layer porous with different diffusion of PTFE in an interdigitated channel. The results also show that the lack of PTFE coatings

can prevent liquid droplets from dropping out even in a small area. Shakernejad et al. [18] investigated the water transfer in a GDL (carbon paper) with a hydrophilic layer using the Boltzmann lattice method. According to the results, the best position to place the hydrophilic layer is the GDL and gas channel(GC). Research shows that the porosity gradient of the GDLs has a significant effect on the performance of the PMFCs, but it is necessary to examine its effect on water management on a pore scale to accurately assess the behavior of liquid water in the GDL. One of the methods that can easily model fluid flow in complex porous media on the pore scale is the LBM. Although the LBM is a successful method for assessing water behavior in the GDLs, there are few studies on the use of the GDL with porosity gradient on water management and improving the performance of PMFCs using this method. In order to achieve a porosity structure that is at least flooded in PMFCs. The runtime on the LBM in porous media is particularly long with fine grids, so using methods to speed up running time is very valuable. Therefore, in this study, the dynamic behavior of liquid water in the GDL of PEMFCs with porosity gradient and without porosity gradient has been evaluated in the pore scale using LBM and the multicomponent Shan-Chen model [19] with GPU implementation (on the graphics card).

2. Numerical simulation

In this study, according to Fig. 1, the D_2 Q_9 Boltzmann lattice scheme is used to model the desired geometry. The probability distribution function of the Streaming process (equation (1)) and the Collision process (equation (2)) for the component σ in the direction f_a^{σ} are based on the Boltzmann lattice equations:

$$f_a^{\sigma,*}(\vec{x}+\vec{e}_a\Delta t,t)=f_a^{\sigma}(\vec{x},t) \quad (1)$$

$$f_a^{\sigma}(\vec{x},t+\Delta t)=f_a^{\sigma,*}(\vec{x},t)-\frac{1}{\tau_\sigma}[f_a^{\sigma,*}(\vec{x},t)-f_a^{\sigma,eq}(\vec{x},t) \quad (2)$$

In the above equations, $f_a^{\sigma,*}$ is the distribution function after the Streaming process, Δt is the grid unit of time, τ_σ the relaxation time of the component, and σ. υ_σ is also the viscosity of the component σ, expressed as $\upsilon_\sigma=c_s^2$ (τ_σ-0.5) Also, based on Fig. 1, discrete velocity $\vec{e}_a$ is expressed as Equation (3):

$$\begin{aligned}&\vec{e}_a=(0,0) \quad , \quad a=0\\&\vec{e}_a=(1,0),(0,1),(-1,0),(0,-1) \quad , \quad a=1,2,3,4\\&\vec{e}_a=(1,1),(-1,1),(-1,-1),(-1,-1) \quad , \quad a=5,2,6,7,8\end{aligned} \quad (3)$$

$$f_a^{\sigma,eq}=w_a\rho_\sigma[1+\frac{\vec{e}_a\vec{u}_\sigma^{eq}}{c_s^2}+\frac{1}{2}(\frac{(\vec{e}_a\vec{u}_\sigma^{eq})^2}{c_s^4}-\frac{\vec{u}_\sigma^{eq}\vec{u}_\sigma^{eq}}{c_s^2})] \quad (4)$$

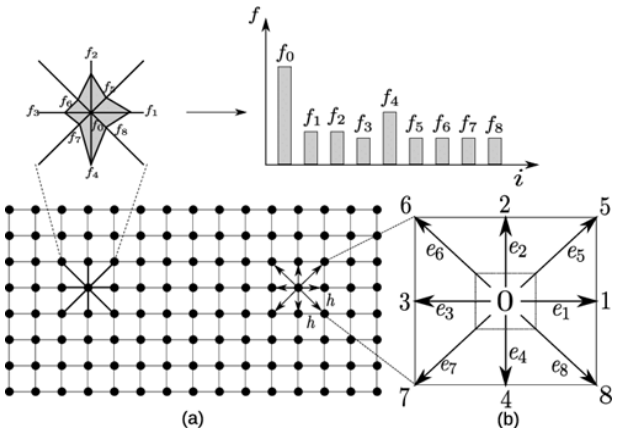

Fig. 1. The D_2 Q_9 Nine-velocity grid model for solving the desired geometry.

The equilibrium distribution function $f_a^{\sigma,eq}$ is also expressed by the BGK form of the Boltzmann equation according to equation (4). The sound velocity c_s for D_2 Q_9 is $1/\sqrt{3}$ and w_a are the discretization coefficients of the Maxwell-Boltzmann equilibrium distribution, which are expressed as follows:

$$w_a=\begin{Bmatrix}4/9 & a=0\\1/9 & a=1-4\\1/36 & a=5-8\end{Bmatrix} \quad (5)$$

The macroscopic fluid density ρ_σ, and velocity $\vec{u}_\sigma$ for each component, the mixture density ρ and the velocity $\vec{u}$ are also calculated from the following equations.

$\rho_\sigma=\sum_a f_a^\sigma$ (6)

$$\vec{u}_\sigma = \frac{1}{\rho_\sigma}\sum_a f_a{}^\sigma \vec{e}_e \quad (7)$$

$\rho=\sum_\sigma \rho_\sigma$ (8)

$$\vec{u} = \frac{\sum_\sigma \rho_\sigma \vec{u}_\sigma / \tau_\sigma}{\sum_\sigma \rho_\sigma / \tau_\sigma} \quad (9)$$

The equilibrium velocity u_σ^{eq} in Equation (4) is also calculated by assuming the momentum exchange rate between fluid-fluid and fluid-solid from the following equation.

$$\rho_\sigma \vec{u}_\sigma^{eq} = \rho_\sigma \vec{u} + \tau_\sigma \sum \vec{F}^\sigma \quad (10)$$

The force $\vec{F}^\sigma$ comprises the adhesion force between two fluids $\vec{F}_{coh}^\sigma(\vec{X})$,the adhesion force between the fluid and the solid surface $\vec{F}_{adh}^\sigma(\vec{x})$ and the external force $\vec{F}_{ext}^\sigma(\vec{x})$ The adhesion force and inter-particle force are also calculated from the following equations:

$$\vec{F}_{coh}^\sigma(\vec{x}) = -\psi_\sigma(\vec{x})\sum_{\bar{\sigma}} G_{c_{\sigma\bar{\sigma}}} \sum_a W_a \psi_{\bar{\sigma}}(\vec{x}+\vec{e}_a\Delta t)\vec{e}_a \quad (11)$$

$$\vec{F}_{adh}^\sigma(\vec{x}) = -\psi_\sigma(\vec{x})\sum_a G_{adh}^\sigma w_a s(\vec{x}+\vec{e}_a\Delta t)\vec{e}_a \quad (12)$$

In equation (11), $\psi_\sigma(\vec{x})$ shows the effective density of the component σ, which can simply be expressed as $\psi_\sigma=\rho_\sigma$. Also, $G_{c_{\sigma\bar{\sigma}}}$ is a controlling surface tension parameter and expresses the interaction between two fluids.

In equation (12), G^σ_{adh} is the adhesion parameter of component σ that can control hydrophobia or hydrophilic fluid against the wall. So that, when G^σ_{adh} is negative, component σ is opposite of hydrophilic surface, and when G^σ_{adh} is positive component σ is opposite of hydrophobia surface. $S(\vec{x}+\vec{e}_a\Delta t)$ is also an index for the presence of a solid barrier around the node and is assigned to values of 0 or 1, respectively, in the presence or absence of a solid lattice sites. P Fluid pressure can be expressed as follows [20].

$$P = \sum \rho_\sigma c_s^2 + \frac{c_s^2}{2}\sum G_{c_{\sigma\bar{\sigma}}}\psi_\sigma(\vec{x})\psi_{\bar{\sigma}}(\vec{x}) \quad (13)$$

3. GPU parallel processing

In recent decades, the use of GPUs to perform non-graphical tasks has attracted the attention of many researchers. Therefore, in recent years, the emergence of new parallel processors has provided a new way to address complex issues such as two-phase flow in porous media by the lattice Boltzmann. Since the LBM does not need to generate a computational grid at any time step, it is easy to program and can be easily programmed on parallel processors such as a graphics card [21]. Kuznik et al. [22] have proposed a method for executing different parts of the LBM on a graphics card. Riegel et al. [23] used a graphics card to simulate the flow around the globe using the LBM . Cheng et al. [24] modeled the two-phase flow of the Shan-Chen model in a tube and showed that the use of GPU parallel processing causes remarkable increase computation.

CUDA (Compute unified device architecture) language is used for programming on the graphics card. (A programming language for graphics computing) The CUDA programming environment is written in two languages, C and C ++, and has all the features of both languages. The CUDA program structure is based on synchronization between the CPU and the GPU, so that, any program written in the CUDA language can have a combination of u commands for the CPU and GPU. Appendix (a) explains the graphic structure and how to allocate memory.

3.1. GPU parallel processing implementation algorithm

The GPU parallel processing computational algorithm in the LBM and their multi-component model are as follows:

- Allocating memory to the graphics card and central processor.
- Allocating initial values related to macroscop-

ic properties and particle positioning function (Porous media) on the central processor.

- Transferring macroscopic properties and particle position function from CPU memory to video card memory.
- Implementation of programmed kernels of LBM in the Shan-Chen multi-component model to solve two-phase flow in porous media and calculating macroscopic properties in the graphics card.
- Transferring the macroscopic properties calculated on the graphics card to the central processor memory.

4. Geometry and simulation conditions

Fig. 2 shows a schematic of the desired geometry along with the boundary conditions and the study areas to simulate water transfer in a GDL of PEMFCs with boundary conditions. The solution area is a 3000Δx × 1800Δx lattice with a thickness GDL thickness of 1080Δx and all three units of lattice has been selected equal to one micrometer (Δx =1μm). Porous media has been randomly by creating solid circular particles of circular shape inside the domain with an the average diameter of circular particles are controlled at 5 μm with a porosity coefficient of 0.659. As shown in Fig. 2, the boundary conditions at the sides have been considered periodic to reduce the size effects. The inlet water enters the GDL located in at the bottom of the catalyst. Assuming that the porosity coefficient of catalyst layer (CL) is equal to 0.2, 100 randomly distributed 2μm pores, water is injected into the GDL. The non-slip boundary condition of the bounce-back algorithm is used to deal with particles. Also, Zou and He conditions is are the boundary conditions at the entry and exit conditions, respectively [25].

Simulation conditions similar to the performance of PEMFCs have been set by non-dimensional numbers. In this simulation, the Reynolds number has been defined as $Re=(\bar{U}d_p)/\vartheta$, ϑ is the fluid kinematic viscosity, d_p is the diameter of the particles from which the porous layer is made, and $\bar{U}$ is the superficial velocity of fluid in the porous media. This small number indicates that the effects of viscosity on the GDL are negligible. Also, the capillary number is defined as $Ca=\bar{U}\mu/\sigma$, (σ is the surface tension) whose small size indicates that capillary force is the reason for water transfer in this geometry, . In addition, due to the low capillary number in the GDL, the effects of large viscosity ratios (~18) and density ratios (~1000) between liquid water and the gas are not important [26].

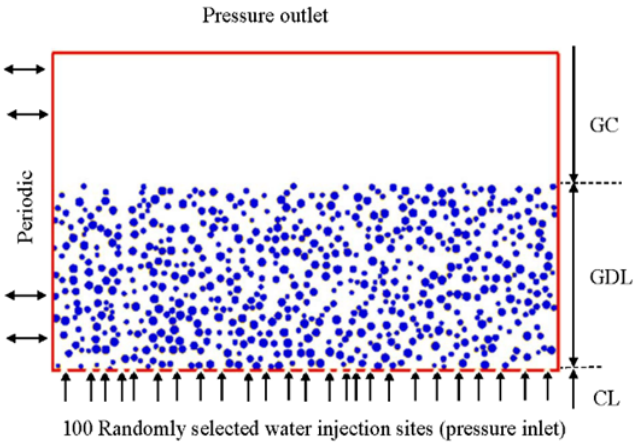

Fig. 2. Schematic of the geometry studied.

5. Validation

Validation of the code written in for three cases (from problems that are analytically resolved) has been performed:

A. Calculation of the permeability of a single phase flow in a porous media using LBM and a comparison with the Kozeny-Carman approx.
B. Calculation of two-phase surface tension using LBM based on Laplace law
C. Modeling of bubble hydrophobia and hydrophilic processes in contact with the solid surface and calculating calculation of the contact angle for different G^{σ}_{adh}

5.1. Calculation of Permeability of Single Phase Flow in Porous Media

Porous media resistance to fluid flow is expressed by a property called permeability, which appears as a coefficient of fitness in Darcy's equation:

$$\bar{U} = -\frac{K}{\vartheta}\nabla p \tag{14}$$

In the above equation, ϑ is the fluid kinematic viscosity, $\bar{U}$ is the superficial fluid velocity in Porous media, K is the permeability, and ∇p is the pressure gradient. The Darcy equation is accurate for flow in porous media and low Reynolds numbers [27]. Using the Kozeny-Carman approximation, we can calculate the permeability coefficient in porous media. We have been calculated of the permeability coefficient K in a porous media with the coefficient ε porosity and d_p particle diameter using the Kozeny-Carman approximation.

$$K = \frac{\varepsilon^3}{180(1-\varepsilon)^2} d^2 \tag{15}$$

It is difficult to estimate the permeability of the GDL against other porous media. So when a measured value of absolute permeability is unavailable, the Carman–Kozeny equation can be used to make an estimate of the GDL [28]. In the Carmen- Kozeny approximation for porous media with a circular structure, the diameter of the pores can be the same as the diameter of the particles [27].

A geometry of 1000Δx×250Δx has been considered to calculate the single phase flow permeability coefficient, using LBM. Each unit of lattice has been selected as one micrometer (Δx=1μm). Porosity gradient is generated by randomly placing solid circular particles with an approximately average diameter of 16 μm with three different porosity coefficients of 0.8, 0.72 and 0.64. As shown in Fig. 2, a uniform flow is assumed to enter the porous media with Re=0.06 (constant velocity condition), and a constant pressure condition is assumed to leave the porous media. No-slip boundary conditions are imposed to the side planes of the domain. The fluid density, ρ, and the relaxation time, τ, which are set to 1.0, are used to simplify the calculation.

The flow permeability values for different porosity coefficients using the LBM are summarized in Table 1 LBM and compared with the Kozeny-Carman approximation and Kim et al. [16]. As can be seen, there is an acceptable congruence between the values obtained by the Kozeny-Carman approximation, especially at high porosity coefficients, which indicates the accuracy of the modeling in porous media. The permeability value obtained from modeling is equivalent to the permeability of carbon paper used as a GDL in PEMFCs [29, 30]. Therefore it can be concluded that the LBM can well model the permeability and behavior of liquid water in the porous media transfer layer of PEMFCs. As the porosity coefficient increases, the error percentage increases because the existing model is a two-dimensional, while the Kozeny-Carman results are extracted for the three-dimensional case.

Table 1. Comparison of calculation of permeability coefficient using LBM, the Kozeny-Carman approximation, and data from Kim et al. [16].

	Flow permeability, K , in the GDLs			
Porosity (ε)	**KC correlation**	**LBM simulation**	**Kim et al. [16]**	**Difference (%)**
0.6	$1.920*10^{-12}\,m^2$	$1.678*10^{-12}m^2$	$1.67*10^{-12}m^2$	12.6%
0.72	$6.771*10^{-12}m^2$	$6.544*10^{-12}m^2$	$6.47*10^{-12}m^2$	3.4%
0.8	$18.25*10^{-12}m^2$	$18.25*10^{-12}m^2$	$17.60*10^{-12}m^2$	2.6%

5-2. Calculation of surface tension of two-phase flow and Laplace law

When one bubble is in another fluid, the surface tension forces resulting from the intermolecular forces in the interface phase of the two liquid and gas phases tend to maintain the bubble stability and tend to minimize the bubble surface. The capillary number ($Ca=(U\bar{}\mu)/\sigma$), which is defined as the ratio of viscosity to surface tension, is very important in two-phase flow and in porous media. Using the Laplace law, we can find the equation between the surface tension σ and the pressure difference ΔP inside and outside the circular bubble, which is inversely proportional to the radius of the bubble R.

$$\Delta p=\sigma/R \tag{16}$$

As shown in Fig. 3, the results are in good agreement with the Laplace law. Fig. 3 shows the bubble surface tension or the slope of the line for. The results are presented using the CPU 0.358 and the GPU 0.364. The small difference between the two methods is because the calculations are done on the GPU up to 8 decimal places but on the CPU up to 16 decimal places.

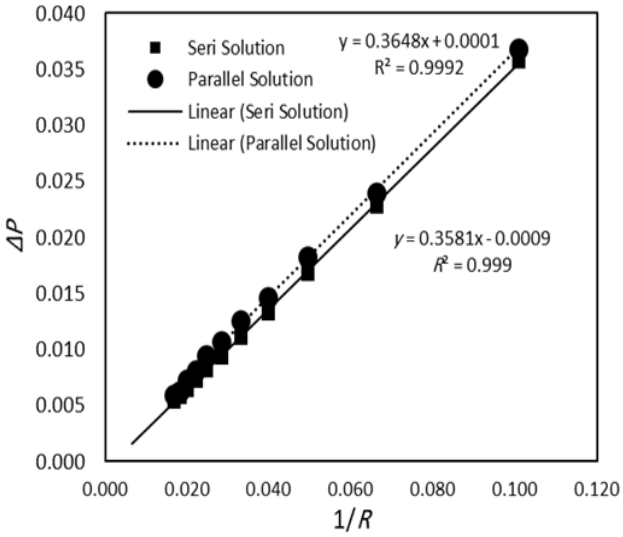

Fig. 3. Correlation between pressure difference and the bubble radius, which is an inverse correlation.

Also, the resolution time for the 200 x 200 lattice and 10,000 replications for the CPU and GPU is provided by a system with an Intel® core i7-7700K processor, GTX 1060 6GB GPU, and 32 system memory, in Table 2. As shown in Table 2, the GPU time is approximately 10 times less compared to the CPU.

Table 2. Comparison of solution time for 200 × 200 lattices for GPU and CPU.

Different processors	Time in seconds
CPU	7.78
GPU	72.6

5-3 Modeling hydrophobia and hydrophilic processes

According to Fig. 4, the area between the solid surface and the two liquid and gas surfaces in the interface phase of the three phase system is called the contact angle. Hydrophobia or hydrophilic surfaces relative to each fluid are expressed using the contact angle, such that if the contact angle is less than 90° the surface is hydrophilic and if the contact angle is greater than 90° the surface is hydrophobia.

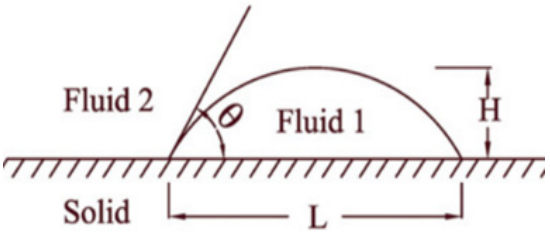

Fig. 4. Definition of contact angle

The contact angle is actually the amount of stress between the two fluids σ and the stress between each phase and the solid surface (σ_{s1},σ_{s2}), which is based on the Young's equation.

$$\cos\theta_c=\frac{\sigma_{s2}-\sigma_{s1}}{\sigma} \tag{17}$$

Assuming a linear relationship between the surface tension, the Young's equation can be expressed as follows [31]. In this study, $G^2_{adh}=-G^1_{adh}$ is considered.

$$\cos\theta_c = \frac{G^2_{adh} - G^1_{adh}}{G_{c_{\sigma\bar{\sigma}}}} \quad (18)$$

Fig. 5 shows the contact angle for different values of G^2_{adh} and its is in good agreement with the Young's equation. As shown in Fig. 5, the negative G^2_{adh} contact angle is less than 90°, indicating that the second component is hydrophilic against the solid surface, and for the positive G^2_{adh} contact angle greater than 90°, indicating tThe hydrophobia donor is the second component versus the solid surface (also for G^1_{adh}).

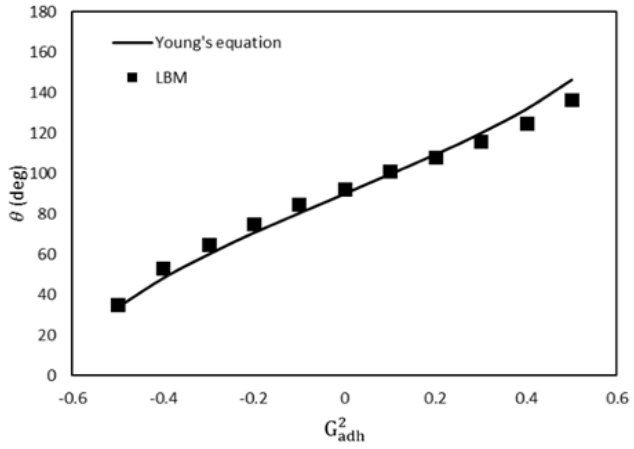

Fig. 5. Contact angle calculated for different values of G^2_{adh}

.

6. Results of GDL water transfer modeling

As mentioned earlier, in this study, Fig. 2 uses two-dimensional porous media to study the flow of water in the porous hydrophobia layer of PEMFCs. For modeling the desired domain is a 3000Δx×1800Δx lattice having a GDL thickness of 1080Δx and a GC thickness of 720Δx. In this range, all three units of lattice are set equal to one micrometer 3Δx=1μm. The different s (GDLs) were constructed using random circles with a mean diameter of 5μm (the average diameter of the circles forming the porous media) and a porosity coefficient of 0.659, as shown in Fig. 6.

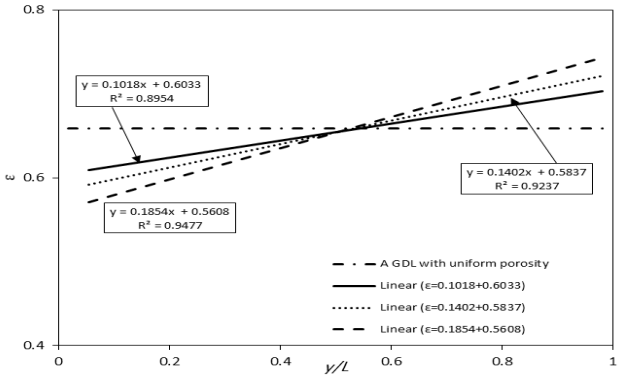

Fig. 6. Comparison of GDLs with same equivalent porosity and different porosity structure, case a: a GDL with uniform porosity, case b: ε=0.1018x+0.6033, case c: ε=0.1402x+0.5837, and case d: ε=0.1854x+0.5608.

6.1. Liquid water transport characteristics

Fig. 7 illustrates the water transfer in a GDL with uniform porosity and contact angle of 106° at different times. According to Fig. 7(a), water from 100 pores to 2μm in diameter passes through the common GDL cathode and the catalyst enters the GDL and then passes through the cathode channel. As it is shown in Fig. 7(a), because of the invasion of liquid water from the 100 injection sites from CL many water clusters are formed inside the porous media d. As shown in Fig. 7(c), the first breakthrough from GDL to GC occurs at 792000 lu and the second breakthrough occurs at 1258000 lu (Fig. 7(d)). Over the time, the number of breakthroughs increases, according to 7(f), with the eighth and last breakthrough occurring at 1716000 lu. Liquid water droplets grow in the interface of GC and GDL, and the droplets merge together to form larger droplets so that at 4500000 lu, the water distribution is stable. In the end, only four big drops remain. In this way, the effect of porosity on the GDL can be attributed to the reduction of the number of breakthroughs from 100 pores at the inlet water to the GDL to 8 sites at the exit of the GDL. The saturation value is defined as the ratio of the volume of liquid water to void volume, which can be expressed locally to obtain profiles or globally to obtain average values.

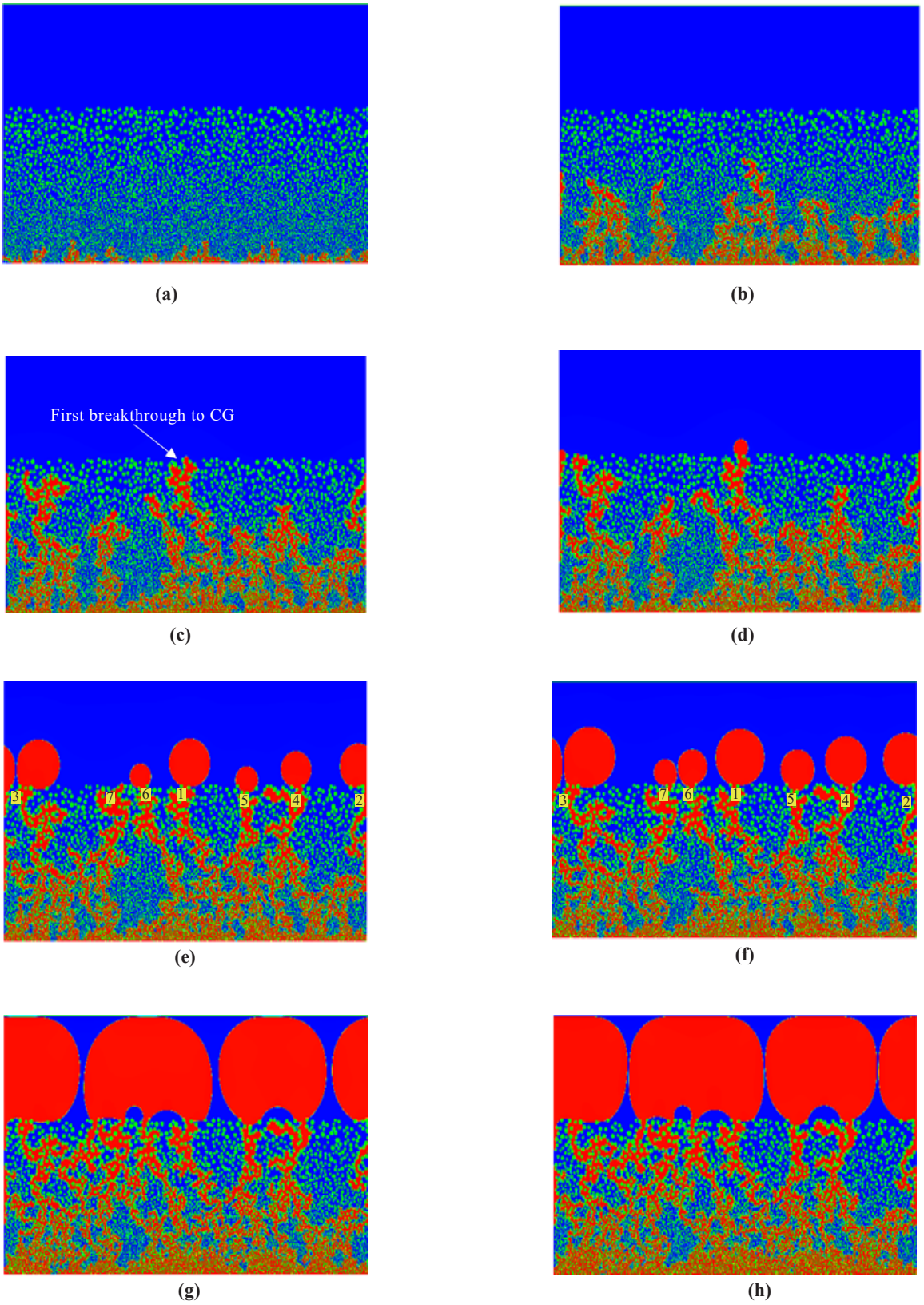

Fig. 7. Evaluation of liquid water cluster in a GDL with uniform porosity: (a) 102000 lu time, (b) 500000 lu time, (c) 792000 lu time, (d) 1258000 lu time, (e) 1580000 lu time, (f) 1716000 lu time, (g) 4005000 lu time, and (h) 4500000 lu time.

Fig. 8 shows the curve of saturation changes along the GDL of the cathode over time. As it can be seen at any point along the length of the GDL, the saturation due to the GDL structure has oscillatory changes and increases with time. Water first flows through paths that have less resistance and then flows through other paths. The increase in saturation over time indicates the gradual filling of the GDL of with the liquid water. The rate of increase in saturation decreases after the first pass at 792000 lu, and this change decreases much more after the last pass at 1716000 lu, at the time of 4500000 lu it reached its steady state and the average saturation value is 0.672.

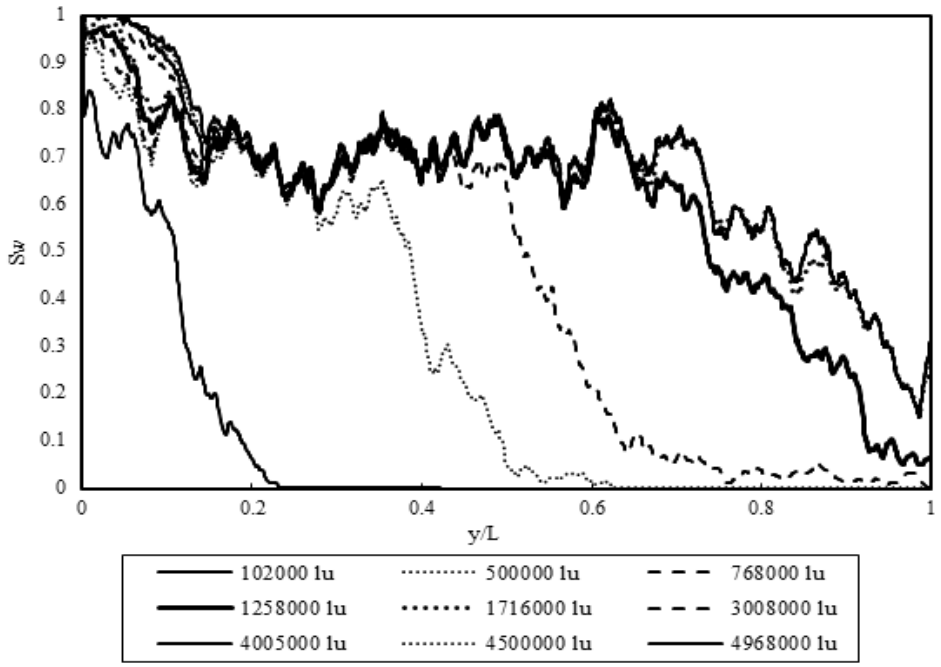

Fig. 8. Temporal evaluation of the liquid saturation profile in a GDL with uniform porosity.

6.2. Effect porosity structure on Liquid water transport

As stated in the introduction, the use of a positive gas porosity gradient GDL can better reduced liquid water in the porous media. Fig. 9 shows the distribution of water in four GDLs. A GDL with uniform porosity and three GDLs with different porosity gradients. As mentioned in the previous section, the thickness of the GDLs is 360μm (1080 Δx) and the average porosity coefficient and mean particle diameter are 0.659 and 5μm, respectively. The contact angle, which indicates the hydrophilic or hydrophobic value of the porous media, is 106 ° for all of the above. This value indicates that all porous layers examined are hydrophobia.

As shown in Fig. 9, the amount of liquid water in the porous layers investigated varies with the porosity structure, the highest value was for the GDL with uniform distribution and the lowest was for the GDL with 18.5% porosity gradient.

The saturation value of water is a parameter that indicates the amount of water in the porosity layer. Fig. 10 shows the saturation distribution curve for the different porosity layers investigated at steady state. As can be seen, the amount of saturation for the GDL with uniform porosity throughout the GDL is almost highest , while the saturation value for the GDL with Porosity gradient is 18.5% is almost lowest .

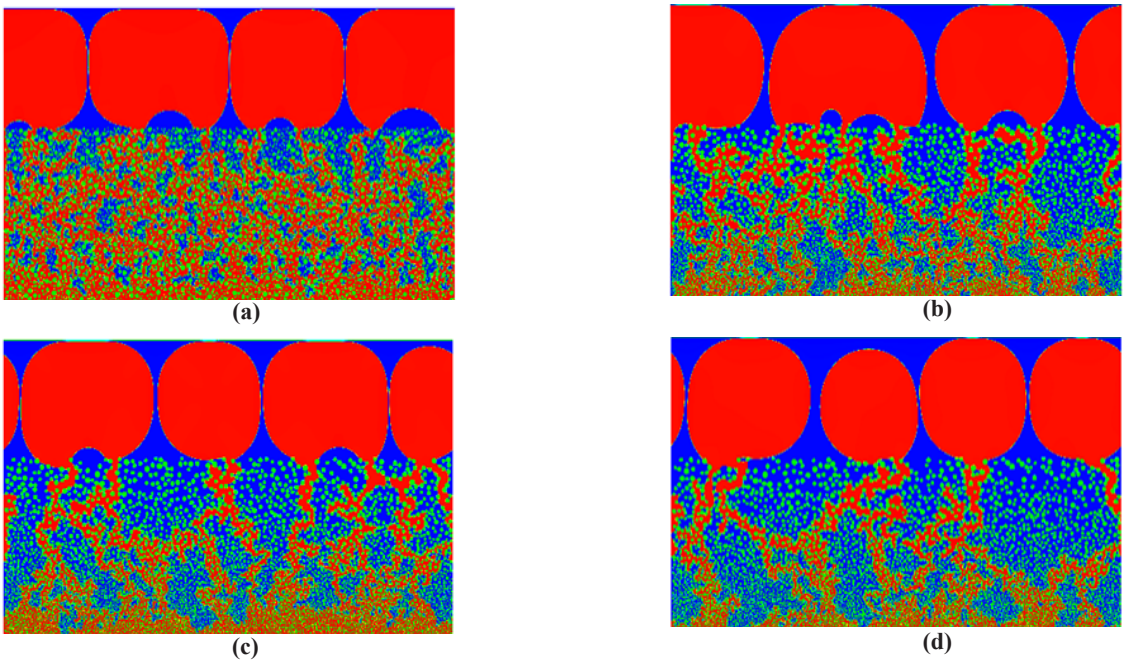

Fig. 9. Steady state distribution of liquid water cluster in GDLs: case a: a GDL with uniform porosity at 4500000 lu time, case b: ε=0.1018x+0.6033 at 7005000 lu time, case c: ε=0.1402x+0.5837 at 7980000 lu time, and case d: ε=0.1854x+0.5608 at 8930000 lu time.

Fig. 11 (a) shows the average saturation value for s GDLs with different structures (with the same porosity coefficient and particle diameter). As it can be seen, the highest average saturation of liquid water for the GDL with uniform porosity is 0.672. Liquid water saturation in the GDLs with porosity gradients of 10%, 14%, and 18.5%, can be reduced by about 20.2%, 29.8%, and 38.8% compared to the GDL with uniform porosity, respectively. Also, according to Fig. 11, theliquid water flow rate for the GDL with a gradient of 14% and 18.5% was 22.3% and 27.2%, respectively, is with less uniform porosity compared to the gas porosity layer GDL.

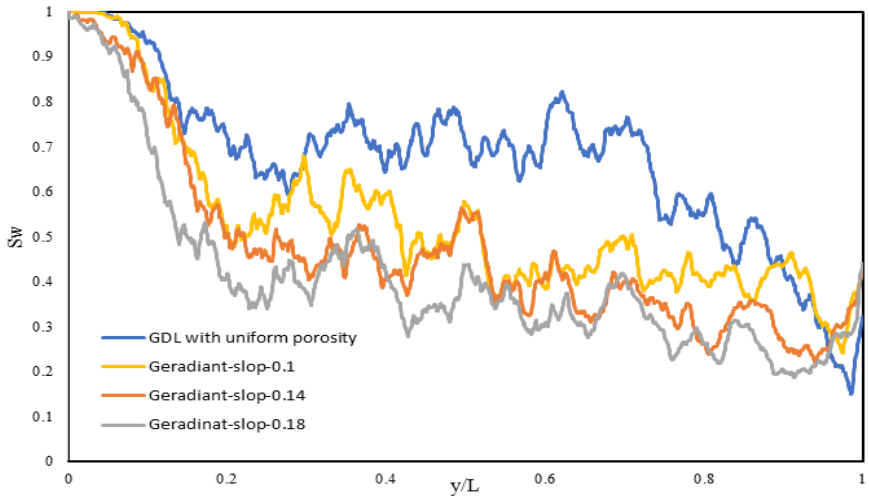

Fig. 10. Steady state liquid saturation profile in GDLs: case a: a GDL with uniform porosity at 4500000 lu time, case b: ε=0.1018x+0.6033 at 7005000 lu time, case c: ε=0.1402x+0.5837 at 7980000 lu time, and case d: ε=0.1854x+0.5608 at 8930000 lu time.

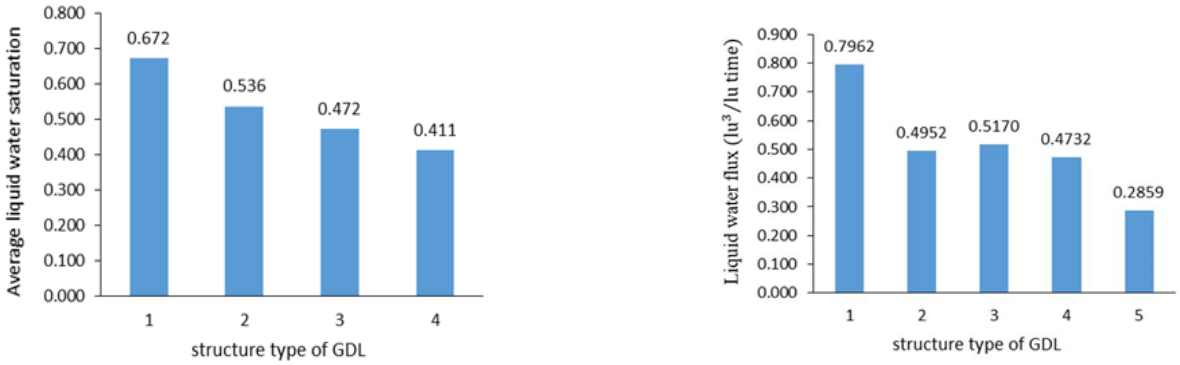

Fig. 11. Comparison of: (a) liquid water remaining in GDL; (b) liquid flux through GDL; case 1: a GDL with uniform porosity, case 2: ε=0.1018x+0.6033, case 3: ε =0.1402x+0.5837, and case 4: ε=0.1854x+0.5608.

7. Conclusions

Water management at high current densities, especially on the cathode side, has a significant effect on the performance of PMFCs. Water management could be facilitated by making GDLs hydrophobic, using MPLs at the GDL-CL interface, and employing GDLs with porosity gradients. This study investigated the effect of porosity gradient in GDL cathode on water transport. The porosity changes in the GDL have been considered linear and have a positive porosity gradient. Because of the complexity of porous media, the pore-scale modeling has been performed by the LBM and the Shan-Chen multiphase and multi-component model. Because in this modeling we have examined the lattice in more detail, in order to reduce the time, calculations have been performed using GPUs using CUDA code. The graphics card processing time was reduced about 17 times compared to the mainframe (for the desired geometry, i.e., a grid with dimensions of 3000Δx×1800Δx.) The written code has been first validated to compute the gas permeability in the GDL and compared with the Kozeny-Carman approximation, then the pressure difference of a static bubble was computed and compared with the Laplace law for surface tension and contact angle calculation in a three-phase system. A phase consisting of a solid medium and two fluid phases by the method near the solid boundary. Investigation of water flow dynamics in GDL with porosity gradient show that:

- In this paper, in addition to quantitative the study of liquid water transfer and distribution within the GDL with porosity gradient were investigated both quantitatively and qualitatively (Figs. 7 & 8) have also been investigated. So that the position of water clusters in the violating times GDL can be observed and described.
- Although water enters the GDL from the large pores of the CL, the water first flows through less resistance paths and discharges through the channel through narrow paths into the GC.
- Flow dynamics in the GDL shows that the water becomes in a drop after it reaches the CG, and the droplets become larger over time. As the droplets grow, the adjacent droplets merge into one another and form larger droplets.
- The dynamic behavior of water in the GDL indicates that over time the average saturation value increased and the local saturation value along the GDL has an oscillatory distribution due to the nature of the GDL.
- The average saturation value in the porosity gradient GDL is less than the uniform porosity GDL; thus, the porosity gradient layer has more free space for transfer of reactions to reaction sites.
- As the porosity gradient increases, the aver-

age saturation in the GDL decreases, but its consumed saturation reduces the electrical resistance in the interface of the GDL and GC increases the resistance to fuel transfer and oxidizer in near catalyst areas.

References

[1] Hassanzadeh, H., A. Ferdowsara, and M. Barzagary, Modeling of two phase flow in the cathode of gas diffusion layer of proton exchange membrane fuel cell. 2014.

[2] Hassanzadeh, H., S.H. Golkar, and M. Barzagary, Modeling of two phase and non-isothermal flow in polymer electrolyte fuel cell. Modares Mechanical Engineering, 2015. 15(2): p. 313-322.

[3] Hassanzadeh, H. and S.H. Golkar, Modeling and Optimization of non-isothermal two-phase flow in the cathode gas diffusion layer of PEM fuel cell. Iranian Journal of Hydrogen & Fuel Cell, 2015. 2(3): p. 159-168.

[4] Zhan, Z., et al., Effects of porosity distribution variation on the liquid water flux through gas diffusion layers of PEM fuel cells. Journal of power sources, 2006. 160(2): p. 1041-1048.

[5] Song, D., et al., Transient analysis for the cathode gas diffusion layer of PEM fuel cells. Journal of Power Sources, 2006. 159(2): p. 928-942.

[6] Gerteisen, D., T. Heilmann, and C. Ziegler, Enhancing liquid water transport by laser perforation of a GDL in a PEM fuel cell. Journal of Power Sources, 2008. 177(2): p. 348-354.

[7] Berning, T. and N. Djilali, A 3D, multiphase, multicomponent model of the cathode and anode of a PEM fuel cell. Journal of the Electrochemical Society, 2003. 150(12): p. A1589-A1598.

[8] Luo, G., H. Ju, and C.-Y. Wang, Prediction of dry-wet-dry transition in polymer electrolyte fuel cells. Journal of The Electrochemical Society, 2007. 154(3): p. B316-B321.

[9] Gurau, V., F. Barbir, and H. Liu, An analytical solution of a half-cell Model for PEM fuel cells. Journal of the Electrochemical Society, 2000. 147(7): p. 2468-2477.

[10] Shi, Z., X. Wang, and O. Draper, Effect of Porosity Distribution of Gas Diffusion Layer on Performance of Proton Exchange Membrane Fuel Cells. ECS Transactions, 2007. 11(1): p. 637-646.

[11] Huang, Y.-X., et al., Effects of porosity gradient in gas diffusion layers on performance of proton exchange membrane fuel cells. Energy, 2010. 35(12): p. 4786-4794.

[12] Lee, C.-I., et al. Effect of Porosity Gradient in Gas Diffusion Layer on Cell Performance With Thin-Film Agglomerate Model in Cathode Catalyst Layer of a PEM Fuel Cell. in ASME 2011 9th International Conference on Fuel Cell Science, Engineering and Technology collocated with ASME 2011 5th International Conference on Energy Sustainability. 2012. American Society of Mechanical Engineers Digital Collection.

[13] Tseng, C.-J. and S.-K. Lo, Effects of microstructure characteristics of gas diffusion layer and microporous layer on the performance of PEMFC. Energy Conversion and Management, 2010. 51(4): p. 677-684.

[14] Oh, H., et al., Effects of pore size gradient in the substrate of a gas diffusion layer on the performance of a proton exchange membrane fuel cell. Applied energy, 2015. 149: p. 186-193.

[15] Chen, F., M.-H. Chang, and P.-T. Hsieh, Two-phase transport in the cathode gas diffusion layer of PEM fuel cell with a gradient in porosity. International Journal of Hydrogen Energy, 2008. 33(10): p. 2525-2529.

[16] Kim, K.N., et al., Lattice Boltzmann simulation of liquid water transport in microporous and gas diffusion layers of polymer electrolyte membrane fuel cells. Journal of Power Sources, 2015. 278: p. 703-717.

[17] Molaeimanesh, G. and M. Akbari, Impact of PTFE distribution on the removal of liquid water from a PEMFC electrode by lattice Boltzmann method. International Journal of Hydrogen Energy, 2014. 39(16): p. 8401-8409.

[18] Shakerinejad, E., et al., Increasing the performance of gas diffusion layer by insertion of small hydrophilic layer in proton-exchange membrane fuel cells. International Journal of Hydrogen Energy, 2018. 43(4): p. 2410-2428.

[19] Shan, X. and H. Chen, Lattice Boltzmann model for simulating flows with multiple phases and components. Physical Review E, 1993. 47(3): p. 1815.

[20] Huang, H., M. Sukop, and X. Lu, Multiphase lattice Boltzmann methods: Theory and application. 2015: John Wiley & Sons.

[21] Li, W., X. Wei, and A. Kaufman, Implementing lattice Boltzmann computation on graphics hardware. The Visual Computer, 2003. 19(7-8): p. 444-456.

[22] Kuznik, F., et al., LBM based flow simulation using GPU computing processor. Computers & Mathematics with Applications, 2010. 59(7): p. 2380-2392.

[23] Riegel, E., T. Indinger, and N.A. Adams, Implementation of a Lattice–Boltzmann method for numerical fluid mechanics using the nVIDIA CUDA technology. Computer Science-Research and Development, 2009. 23(3-4): p. 241-247.

[24] Cheng, P., et al., Application of lattice Boltzmann methods for the multiphase fluid pipe flow on graphical processing unit. The Journal of Computational Multiphase Flows, 2018. 10(3): p. 109-118.

[25] Zou, Q. and X. He, On pressure and velocity boundary conditions for the lattice Boltzmann BGK model. Physics of fluids, 1997. 9(6): p. 1591-1598.

[26] Mukherjee, P.P., C.-Y. Wang, and Q. Kang, Mesoscopic modeling of two-phase behavior and flooding phenomena in polymer electrolyte fuel cells. Electrochimica Acta, 2009. 54(27): p. 6861-6875.

[27] Kaviany, M., Principles of heat transfer in porous media. 2012: Springer Science & Business Media.

[28] Mench, M.M., Fuel cell engines. 2008: John Wiley & Sons.

[29] Feser, J., A. Prasad, and S.G. Advani, Experimental characterization of in-plane permeability of gas diffusion layers. Journal of power sources, 2006. 162(2): p. 1226-1231.

[30] Gostick, J.T., et al., In-plane and through-plane gas permeability of carbon fiber electrode backing layers. Journal of Power Sources, 2006. 162(1): p. 228-238.

[31] Sukop, M., DT Thorne, Jr. Lattice Boltzmann Modeling Lattice Boltzmann Modeling. 2006: Springer.

[32] Tölke, J., Implementation of a Lattice Boltzmann kernel using the Compute Unified Device Architecture developed by nVIDIA. Computing and Visualization in Science, 2010. 13(1): p. 29.

Appendix A

A.1 Graphics Card Structure

The graphics card is subdivided into several subsets to execute the recall functions. Each of the subsets can perform a recall function. Kernel is considered as a function that is recalled to run on the graphics card. When a function (kernel) is recalled, many threads are organized by the graphics card to simultaneous execute the function. The processor is the smallest executable unit which executes some kernels on the graphics card. These running units are almost similar to the CPUs, but they are much larger. The CUDA programming language classifies CPU processing threads into two general levels to organize and classify them. The first class is Block, in which the blocks have a very strong shared memory that enables the processing threads in that block to be con-

nected and synchronized. The position of processing threads within a block is specified by the ThreadIdx of that thread, and this property can be defined in one, two, and three-dimensional formulas. The maximum processing threads within a block depends on the physical structure of the graphics card. In today's graphics cards, blocks can accommodate up to 1024 processing threads. The second level is called Grid, which contains a set of blocks. Unlike the processing threads within a block, processing threads in different blocks cannot be matched. The position of blocks is also specified by the BlockIdx index on the grid like processing threads (Fig. 12).

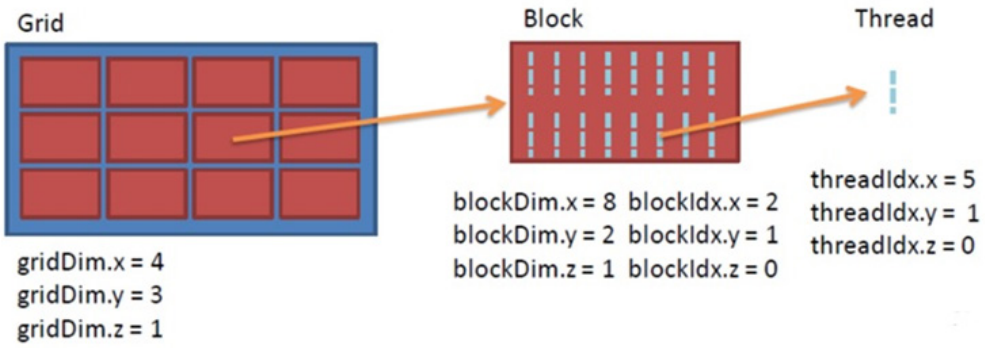

Fig. 12. Organize and classify processors for mainframe processing and coding programming.

Blocks can also be arranged in two-dimensional or three-dimensional form. As mentioned, the maximum number of processing threads within a block depends on the physical structure of the graphics card and is somewhat limited but the number of blocks is almost unlimited. Generally, when a kernel is called to run on the graphics card, a set of processing threads is organized within a grid of blocks to execute the desired kernel. As shown in Fig. 12, when kernel No.1 is recalled, processing threads inside the blocks are arranged in 3D. The number of blocks and processing threads is specified by the programmer in the kernel recall.

One of the most important issues in using a graphics card is the processing of threads in a grid in such a way that it fits with the desired computational grid. In this article, the processing threads, i.e., the computational grid, have been arranged in a two-dimensional form (Fig. 13), and each computational node is performed in a LBM by a processing thread.

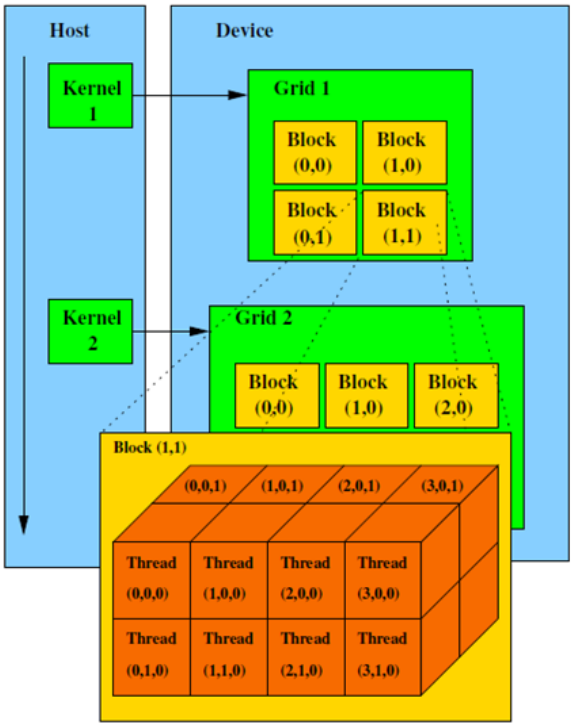

Fig. 13. Schematic of the layout of the processors in the graphics card.

A.2 Memory allocation

The central processing unit (CPU) and graphics card have separate memory. To run a kernel on the graphics card, the developer must have a decent amount of memory on the graphics card to perform allocate calculations and then transfer the relevant information from the system memory to the memory allocated on the graphics card, and finally, after doing the calculations, transfer the results to the main memory and free up the memory on the graphics card. The graphics card's general memory is accessible to the CPU unit, so that, it can transfer information to the graphics card. API (Application programming Interface) functions are needed to allocate graphics card memory or transfer memory to the CPU and graphics card [32].